Journal of the Optical Society of America A
OPTICS, IMAGE SCIENCE, AND VISION

Frequency shift between near- and far-field scattering resonances in dielectric particles

Alex J. Yuffa,[1,*] Yael Gutierrez,[2] Juan M. Sanz,[2] Rodrigo Alcaraz de la Osa,[2] José M. Saiz,[2] Francisco González,[2] Fernando Moreno,[2] and Gorden Videen[1,2,3]

[1]Computational & Information Science Directorate, Army Research Laboratory, Adelphi, Maryland 20783, USA
[2]Grupo de Óptica, Departamento de Física Aplicada, Universidad de Cantabria, Facultad de Ciencias, Avda. Los Castros s/n, 39005 Santander, Spain
[3]Instituto Nacional de Técnica Aerospacial (INTA), Ctra. Ajalvir Km. 4, 28850 Torrejón de Ardoz, Madrid, Spain
*Corresponding author: ayuffa@gmail.com

Received 29 April 2015; revised 17 July 2015; accepted 18 July 2015; posted 20 July 2015 (Doc. ID 238568); published 12 August 2015

The near-field electromagnetic scattering intensity resonances are redshifted in frequency with respect to their far-field counterparts. We derive simple, approximate, analytical formulas for this shift in the case of a plane wave interacting with a dielectric sphere. Numerical results comparing the approximate formulas to the numerically exact solutions show that the two are in good agreement. We also consider the Rayleigh limit of the formulas to gain more insight into the phenomenon.

OCIS codes: (220.4241) Nanostructure fabrication; (310.6628) Subwavelength structures, nanostructures; (260.5740) Resonance; (290.5870) Scattering, Rayleigh.

http://dx.doi.org/10.1364/JOSAA.32.001638

1. INTRODUCTION

With recent technological advances it has become possible to control light at the nanoscale through the use of nanoparticles and nanostructures, e.g., see [1] and references therein. At this scale, quantities of interest are related to the near-field intensity as opposed to the conventional far-field quantities, such as the scattering and absorption cross sections, or far-field intensities. In metallic particles, localized surface plasmon resonances allow for subwavelength confinement of an incident electromagnetic wave and for large enhancement of the field near the surface of the nanoparticle. These properties are particularly important from an applied perspective as they are utilized in many different application arenas such as biosensing [2], surface-enhanced Raman spectroscopy [3], and nanometric optical trapping [4]. One especially relevant application is designing and tuning nanoparticle resonances to be used as sources or detectors. If the nanoparticle system is designed using far-field solutions, the resulting device that is used in the near field will not be optimized.

Recently, a redshift of the near-field intensity peaks with respect to the intensity peaks in the far field has attracted attention [5–10]. In principle, a qualitative understanding and a quantitative prediction of this redshift would allow for an optimization of the near fields based on their far-field counterparts, which are generally easier to measure. On the conceptual front, the redshift of metallic particles has been explained in terms of a damped harmonic oscillator model, where the maximum of the kinetic and dissipation energies occur at the natural frequency of the oscillator, but the maximum of the potential energy occurs at a lower frequency due to a nonzero damping constant [5–7]. If we associate the far-field cross sections with the kinetic and dissipation energies and the near-field intensity with the potential energy ($\propto$ amplitude), then we see how the oscillator model qualitatively explains the origin of the redshift in highly absorbent nanoparticles. It has been noted by Chen *et al.* [5] that the damping may not be the only factor causing the redshift. In fact, Moreno *et al.* [9] recently demonstrated that evanescent waves contribute to the redshift of metallic particles. This suggests that the redshift also will occur in the light scattered by dielectric nanoparticles because an incident wave may excite the internal resonances of the particle, thereby generating the evanescent waves emanating from the surface of the particle [11]. We use this physical insight to derive relatively simple analytical formulas for the redshift between the far- and the near-field intensity peaks of the light scattered by a dielectric sphere. These formulas not only accurately predict the redshift, but also offer further physical insight into the phenomenon by explicitly showing the dependence of the redshift on the physical parameters of the system. It should be noted that high permittivity dielectric nanoparticles, e.g., silicon spheres, are of current research interest because they can have strong resonances over different spectral regions, which can be desirable for varied applications, e.g., dielectric metamaterials [12–14].

Table 1. Brief Description of the Symbols Used Throughout the Paper

Symbol	Description
j_n	Spherical Bessel function of the 1st kind
y_n	Spherical Bessel function of the 2nd kind
h_n	Spherical Hankel function of the 1st kind
$\psi_n(\eta) = \eta j_n(\eta)$	Riccati–Bessel function
$\chi_n(\eta) = -\eta y_n(\eta)$	Riccati–Bessel function
$\eta(\eta) = \eta h_n(\eta)$	Riccati–Bessel function
P_n^m	Associated Legendre polynomial with the Condon–Shortley phase
c	Speed of light in vacuum
ϵ_1	Permittivity of the host space (Region 1)
ϵ_2	Permittivity of the sphere (Region 2)
$k_1 = \sqrt{\epsilon_1}\frac{\omega}{c}$	Wavenumber in Region 1
$k_2 = \sqrt{\epsilon_2}\frac{\omega}{c}$	Wavenumber in Region 2

Throughout this paper, we use the Gaussian unit system and assume that all fields are harmonic in time with a $\exp(-i\omega t)$ time factor, where ω is the angular frequency. For simplicity we assume that the scatterer and the host space have the same permeability. Furthermore, for the reader's convenience a partial list of the symbols used in the paper is presented in Table 1.

2. REDSHIFT FORMULA

If a monochromatic plane wave of unit amplitude propagating in the $\hat{\mathbf{z}}$-direction and polarized in the $\hat{\mathbf{x}}$-direction is incident on a sphere of radius ρ, then the scattered partial-wave electric field is given by

$$\mathbf{E}_n(r,\theta,\phi) = -\frac{2n+1}{n(n+1)} i^n (A_n \mathbf{M}_{1n} - iB_n \mathbf{N}_{1n}), \tag{1a}$$

where

$$\mathbf{M}_{1n} = \frac{1}{\sin\theta} h_n(\eta) P_n^1(\cos\theta)\cos\phi\hat{\boldsymbol{\theta}} - h_n(\eta)\frac{\mathrm{d}}{\mathrm{d}\theta}P_n^1(\cos\theta)\sin\phi\hat{\boldsymbol{\phi}}, \tag{1b}$$

$$\mathbf{N}_{1n} = \frac{n(n+1)}{\eta} h_n(\eta) P_n^1(\cos\theta)\cos\phi\hat{\mathbf{r}} + \frac{1}{\eta}\frac{\mathrm{d}}{\mathrm{d}\eta}[\eta h_n(\eta)]\frac{\mathrm{d}}{\mathrm{d}\theta}P_n^1(\cos\theta)\cos\phi\hat{\boldsymbol{\theta}} - \frac{1}{\eta\sin\theta}\frac{\mathrm{d}}{\mathrm{d}\eta}[\eta h_n(\eta)]P_n^1(\cos\theta)\sin\phi\hat{\boldsymbol{\phi}}, \tag{1c}$$

and $\eta = k_1 r$, where r is the radial distance and k_1 is the wavenumber in Region 1, θ is the polar angle, and ϕ is the azimuthal angle. In Eq. (1a), the partial scattering amplitudes are given by

$$A_n = -\frac{a_n}{a_n - ic_n} \quad \text{and} \quad B_n = -\frac{b_n}{b_n - id_n}, \tag{2a}$$

where

$$a_n = \frac{k_2}{k_1}\psi_n(k_1\rho)\psi_n'(k_2\rho) - \psi_n'(k_1\rho)\psi_n(k_2\rho), \tag{2b}$$

$$c_n = \frac{k_2}{k_1}\chi_n(k_1\rho)\psi_n'(k_2\rho) - \chi_n'(k_1\rho)\psi_n(k_2\rho), \tag{2c}$$

$$b_n = \psi_n(k_1\rho)\psi_n'(k_2\rho) - \frac{k_2}{k_1}\psi_n'(k_1\rho)\psi_n(k_2\rho), \tag{2d}$$

$$d_n = \chi_n(k_1\rho)\psi_n'(k_2\rho) - \frac{k_2}{k_1}\chi_n'(k_1\rho)\psi_n(k_2\rho), \tag{2e}$$

and the prime denotes differentiation with respect to the argument. If we define the angularly integrated scattered intensity as

$$\tilde{I}_n(\omega, r) = \int_0^{2\pi}\int_0^{\pi} \mathbf{E}_n(r,\theta,\phi)\cdot\mathbf{E}_n^*(r,\theta,\phi)\sin\theta \mathrm{d}\theta\mathrm{d}\phi, \tag{3}$$

where * denotes the complex conjugate, then by substituting Eq. (1) into Eq. (3), and using the orthogonality properties of $\mathbf{M}_{1n}$ and $\mathbf{N}_{1n}$, we obtain

$$\tilde{I}_n(\omega, r) = \frac{2\pi}{\eta^2} I_n(\omega, r), \tag{4a}$$

where

$$I_n(\omega, r) = |A_n(\omega)|^2 g_n^{\mathrm{m}}(\omega, r) + |B_n(\omega)|^2 g_n^{\mathrm{e}}(\omega, r), \tag{4b}$$

$$g_n^{\mathrm{m}} = (2n+1)\eta^2 |h_n(\eta)|^2, \tag{4c}$$

and

$$g_n^{\mathrm{e}} = \eta^2((n+1)|h_{n-1}(\eta)|^2 + n|h_{n+1}(\eta)|^2). \tag{4d}$$

From here on we choose to work with the normalized intensity $I_n(\omega, r)$ instead of $\tilde{I}_n(\omega, r)$ because the normalized intensity $I_n(\omega, r)$ reduces to a convenient form in the far field; namely,

$$I_n(\omega) = (2n+1)(|A_n(\omega)|^2 + |B_n(\omega)|^2), \qquad \eta \gg 1, \tag{5a}$$

where

$$|A_n|^2 = \frac{a_n^2}{a_n^2 + c_n^2} \quad \text{and} \quad |B_n|^2 = \frac{b_n^2}{b_n^2 + d_n^2}. \tag{5b}$$

With this normalization, the far-field intensity does not depend on the radial distance r and thus, the far-field intensity resonances are also independent of r. Of course, we have obtained Eq. (5) from Eq. (4) by simply using the asymptotic form of the spherical Hankel functions.

From Eq. (1), we see that the A_n (B_n) coefficients are the amplitudes of oscillations of the magnetic (electric) type. Analogously, we say that a far-field resonance is of the magnetic or electric type if A_n or B_n are maximum. Let us denote these magnetic (electric) resonant frequencies by ω_ℓ^{m} (ω_ℓ^{e}) and their near-field counterparts by $\tilde{\omega}_\ell^{\mathrm{m}}$ ($\tilde{\omega}_\ell^{\mathrm{e}}$). Here the subscript $\ell = 1, 2, \ldots$ is simply used to label each resonant frequency and does not imply any particular ordering. To find ω_ℓ^{m}, we require the derivative of $|A_n|^2$ with respect to ω to vanish, which yields

$$a_n = 0, \qquad c_n = 0, \qquad \text{or} \qquad \frac{\mathrm{d}a_n}{\mathrm{d}\omega}c_n + a_n\frac{\mathrm{d}c_n}{\mathrm{d}\omega} = 0. \tag{6}$$

From the functional form of $|A_n|^2$ given in Eq. (5b), we see that the maximum occurs whenever $c_n = 0$. In other words, ω_ℓ^{m} are the solutions to the transcendental equation $c_n = 0$. Similarly, ω_ℓ^{e} are the solutions to the transcendental equation $d_n = 0$. We may consider the magnetic and the electric type resonances separately because c_n and d_n coefficients do not vanish simultaneously. Thus, it is convenient to decompose the total scattered intensity [Eqs. (4)] into its magnetic and electric contribution; namely, $I_n(\omega, r) = I_n^{\mathrm{m}}(\omega, r) + I_n^{\mathrm{e}}(\omega, r)$, where

$$I_n^{\mathrm{m}}(\omega, r) = |A_n(\omega)|^2 g_n^{\mathrm{m}}(\omega, r), \tag{7a}$$

$$I_n^{\mathrm{e}}(\omega, r) = |B_n(\omega)|^2 g_n^{\mathrm{e}}(\omega, r). \tag{7b}$$

While this provides a convenience in description, we note that this expression may not be practical for applications, as the location of a particular resonance may appear shifted due to the presence of the additional modes. In practice, this effect can be reduced or eliminated by illuminating or detecting only the polarization component of the resonance of interest. Furthermore, from Eq. (4d) we see that $g_{n=1}^{\mathrm{e}}(\omega, r)/k_1^2$ scales as $1/k_1^6$ and, thus, Eq. (7b) is in agreement with the universal incident wavelength dependence predicted by Moreno *et al.* [9].

3. ELECTRIC REDSHIFT FORMULAS

The redshift formula for the electric or magnetic resonances may be derived by exploiting a particular functional form of the partial scattering amplitudes, as shown in Appendix A. In the case of the electric redshift, we let $\omega_0 = \omega_\ell^{\mathrm{e}}$, $\mathbb{A} = b_n$, $\mathbb{B} = d_n$, and $g = g_n^{\mathrm{e}}$ in Eq. (A2) to obtain

$$\Delta\omega_\ell^{\mathrm{e}}(r) = \tilde{\omega}_\ell^{\mathrm{e}}(r) - \omega_\ell^{\mathrm{e}} \approx \frac{1}{2}\frac{\dot{g}_n^{\mathrm{e}}(\omega_\ell^{\mathrm{e}}, r)}{g_n^{\mathrm{e}}(\omega_\ell^{\mathrm{e}}, r)}\left[\frac{b_n(\omega_\ell^{\mathrm{e}})}{\dot{d}_n(\omega_\ell^{\mathrm{e}})}\right]^2, \tag{8}$$

where the overdot $\cdot$ denotes differentiation with respect to ω. The redshift formula [Eq. (8)] allows us to rapidly and accurately calculate how the far-field electric intensity resonances depend on radial distance r. To demonstrate the accuracy of Eq. (8) we have listed the relative error associated with it in Table 2. In the table we have identified the far-field resonant frequencies using the unitless electric size parameter x_ℓ^{e} instead of ω_ℓ^{e}, i.e., $x_\ell^{\mathrm{e}} = \sqrt{\epsilon_1}\rho\omega_\ell^{\mathrm{e}}/c$, and evaluated the near-field resonance $\tilde{\omega}_\ell^{\mathrm{e}}(r)$ on the surface of the sphere $r = \rho$. Furthermore, to demonstrate how the relative error depends on radial distance, we have plotted the relative error as a function of the scaled radial distance for a number of worst-case scenario resonances in Fig. 1. From these data we see that the relative error is generally very small and tends to decrease with radial distance. This is expected behavior as the redshift should increase near the surface of the particle, where the evanescent wave contribution is greatest (see Fig. 2).

Table 2. Relative Errors Associated with Using Eq. (8) for a Sphere with a Dielectric Constant of 10

n	ℓ	x_ℓ^{e}	Rel. Error in %
1	1	0.44404161231126	3.40×10^{-2}
1	2	0.76111381942357	9.14×10^{-1}
1	3	1.0730776730363	4.45
1	4	1.3888710632302	5.07
1	5	1.7085740733775	2.12
1	6	2.0284063829955	6.33×10^{-1}
1	7	2.3472206484602	1.66×10^{-1}
1	8	2.6652685984771	1.99×10^{-2}
1	9	2.9830223110202	3.88×10^{-2}
2	10	0.57329872365611	2.89×10^{-5}
2	11	0.90414933943808	2.59×10^{-3}
2	12	1.2237952354462	4.89×10^{-2}
2	13	1.5386833689535	3.99×10^{-1}
2	14	1.8515469192830	1.61
2	15	2.1657001377980	3.07
2	16	2.4832719779298	2.73
2	17	2.8029458320520	1.41

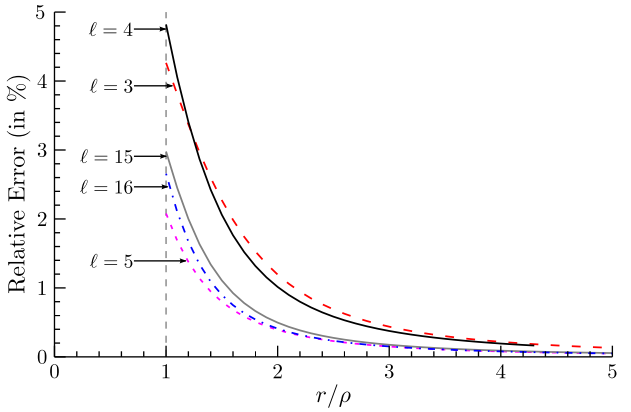

Fig. 1. Relative error associated with the redshift formula [Eq. (8)] is shown as a function of the scaled radial distance for several resonances listed in Table 2.

To gain further insight into Eq. (8), we consider the Rayleigh limit. Namely, substituting

$$\psi_1(x) = \frac{1}{3}x^2 - \frac{1}{30}x^4 + O(x^6), \tag{9a}$$

$$\chi_1(x) = \frac{1}{x} + \frac{x}{2} - \frac{1}{8}x^3 + O(x^5), \tag{9b}$$

and

$$\psi_1'(x) = \frac{2}{3}x - \frac{2}{15}x^3 + O(x^5), \tag{9c}$$

$$\chi_1'(x) = -\frac{1}{x^2} + \frac{1}{2} - \frac{3}{8}x^2 + O(x^4), \tag{9d}$$

into Eqs. (2d) and (2e) yields

$$b_1 \approx \frac{2}{9}x_2(x_1^2 - x_2^2), \tag{10a}$$

$$\dot{d}_1 \approx -\frac{x_1 x_2}{15\omega}\left[\left(\frac{x_2}{x_1}\right)^4 + 9\left(\frac{x_2}{x_1}\right)^2 + 10\right], \tag{10b}$$

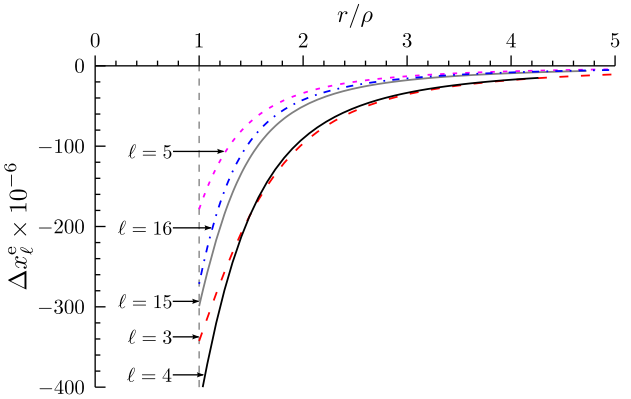

Fig. 2. Scaled redshift $\Delta x_\ell^{\mathrm{e}}$ is plotted as a function of the scaled radial distance for several resonances listed in Table 2.

where $x_1 = \sqrt{\epsilon_1}\rho\omega/c$ and $x_2 = \sqrt{\epsilon_2}\rho\omega/c$. Using the sum of squares formula for the spherical Bessel functions ([15], Section 10.49(iv))

$$j_n^2(x) + y_n^2(x) = \sum_{p=0}^{n} \frac{S_p(n)}{x^{2p+2}}, \tag{11a}$$

where

$$S_p(n) = \begin{cases} \frac{(2p)!(n+p)!}{2^{2p}(p!)^2(n-p)!}, & p = 0, 1, \ldots, n \\ 0, & p > n \end{cases}, \tag{11b}$$

to rewrite Eq. (4d) as

$$g_n^{\mathrm{e}}(x) = \sum_{p=0}^{n+1} \frac{(n+1)S_p(n-1) + nS_p(n+1)}{x^{2p}}, \tag{12}$$

and then substituting Eqs. (10) and (12) into Eq. (8) finally yields the desired formula:

$$\Delta\omega_{\ell,n=1}^{\mathrm{e}} \approx -\frac{\eta^2+6}{\eta^4+\eta^2+3}\left(\frac{10x_1^3}{3x_2^2+30x_1^2}\right)^2 \omega_\ell^{\mathrm{e}}, \tag{13a}$$

when $\{x_1, x_2\} \ll 1$ and $x_1 \neq x_2$. The negative sign on the right-hand side of Eq. (13a) confirms that the near-field intensity peaks are indeed redshifted with respect to their far-field counterparts. We also see that $\Delta\omega_{\ell,n=1}^{\mathrm{e}}$ is inversely proportional to the fourth power of the refractive index of the sphere if $x_2 > x_1$. Furthermore, we note that the higher order redshifts can be derived in an analogous manner; for example, the quadrupole redshift is given by

$$\Delta\omega_{\ell,n=2}^{\mathrm{e}} \approx -\frac{3(\eta^4+12\eta^2+90)}{\eta^6+3\eta^4+18\eta^2+90}\left(\frac{7x_1^5}{30x_2^2+105x_1^2}\right)^2 \omega_\ell^{\mathrm{e}}. \tag{13b}$$

4. MAGNETIC REDSHIFT FORMULAS

Proceeding analogously to Section 3, we obtain

$$\Delta\omega_\ell^{\mathrm{m}}(r) = \tilde{\omega}_\ell^{\mathrm{m}}(r) - \omega_\ell^{\mathrm{m}} \approx \frac{1}{2}\frac{\dot{g}_n^{\mathrm{m}}(\omega_\ell^{\mathrm{m}}, r)}{g_n^{\mathrm{m}}(\omega_\ell^{\mathrm{m}}, r)}\left[\frac{a_n(\omega_\ell^{\mathrm{m}})}{\dot{c}_n(\omega_\ell^{\mathrm{m}})}\right]^2, \tag{14}$$

Table 3. Relative Errors Associated with Using Eq. (14) for a Sphere with a Dielectric Constant of 10

n	ℓ	x_ℓ^{m}	Rel. Error in %
1	1	0.31130447515856	7.94×10^{-3}
1	2	0.62398570479241	6.50×10^{-2}
1	3	0.93834713028058	1.54×10^{-1}
1	4	1.2540335431079	2.42×10^{-1}
1	5	1.5707963267949	3.53×10^{-1}
1	6	1.8889337144859	5.93×10^{-1}
1	7	2.2102197037432	1.48
2	8	0.44775047977432	2.55×10^{-5}
2	9	0.76961156442652	1.21×10^{-3}
2	10	1.0862284580243	1.09×10^{-2}
2	11	1.4015575650554	4.14×10^{-2}
2	12	1.7168078189283	9.43×10^{-2}
2	13	2.0324277448812	1.61×10^{-1}
2	14	2.3485738549284	2.44×10^{-1}
2	15	2.6653903766980	3.72×10^{-1}
2	16	2.9832885136309	6.52×10^{-1}

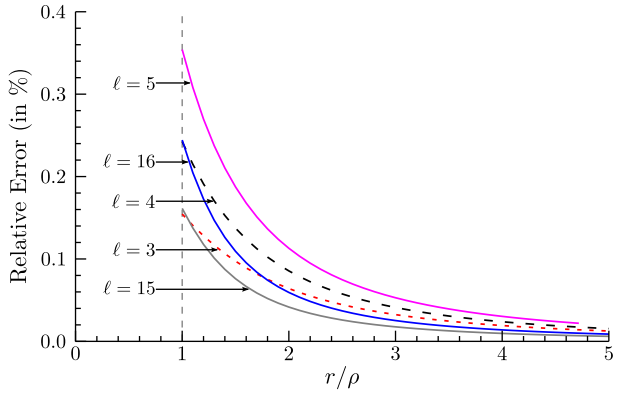

Fig. 3. Relative error associated with the redshift formula [Eq. (14)] is shown as a function of the scaled radial distance for several resonances listed in Table 3.

which is the redshift formula for the magnetic resonances. As in Section 3, we tabulate the relative error associated with Eq. (14) when $r = \rho$ and plot the relative error as a function of the scaled radial distance for several resonances; see Table 3 and Fig. 3, respectively. By comparing Table 2 and Fig. 1 with Table 3 and Fig. 3, respectively, we see that the relative error is generally smaller for the magnetic case than the electric case. This is expected as the associated redshift is also smaller in the magnetic case; see Figs. 2 and 4. Furthermore, by comparing

$$\Delta\omega_{\ell,n=1}^{\mathrm{m}} \approx -\frac{x_1^6}{225(\eta^2+1)}\omega_\ell^{\mathrm{m}} \tag{15a}$$

and

$$\Delta\omega_{\ell,n=2}^{\mathrm{m}} \approx -\frac{(\eta^2+6)x_1^{10}}{33075(\eta^4+3\eta^2+9)}\omega_\ell^{\mathrm{m}} \tag{15b}$$

to Eqs. (13a) and (13b), respectively, we see that, in the Rayleigh limit, the magnetic dipole and quadrupole redshifts are much smaller than their electric counterparts. Of course, if we consider the magnetic intensity instead of the electric intensity, then the situation would be reversed because the role of A_n and B_n are reversed, as well.

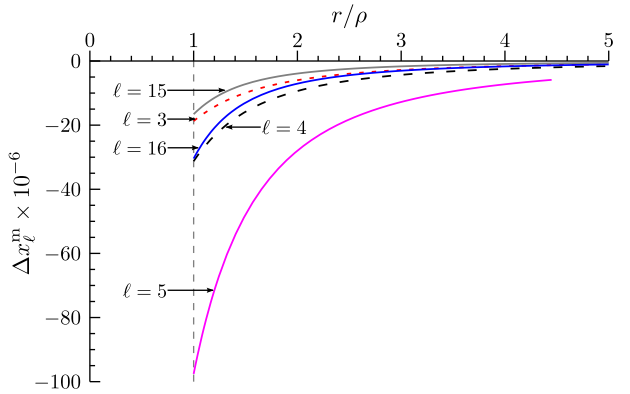

Fig. 4. Scaled redshift $\Delta x_\ell^{\mathrm{m}}$ is plotted as a function of the scaled radial distance for several resonances listed in Table 3.

5. CONCLUSIONS

We have developed approximate formulas for predicting the redshift between the near-field electric intensity peaks and their far-field counterparts. These formulas were derived for a plane wave scattering from a dielectric sphere. Through numerical examples we have demonstrated that these formulas accurately predict the redshift. Furthermore, we considered the Rayleigh limit of the formulas and deduced that the redshifts associated with the magnetic resonances are orders of magnitude smaller than their electric counterparts.

Recently it was demonstrated that the resonances in weakly lossy dielectric particles are only slightly affected by the losses [16]. Although our approach is valid only for ideal dielectric scatterers, we speculate that it may be possible to extend it to weakly absorbing scatterers by expanding the Riccati–Bessel functions in the small absorption parameter, as was done in [17]. The benefit of such an expansion is that we will approximately retain the functional form of the absolute value squared of the partial scattering amplitudes, and, therefore, we will be able to build on the derivation presented in this paper. We will further discuss this possibility in the future.

APPENDIX A: NEAR- AND FAR-FIELD PEAKS

If a function of the form

$$I(\omega, r) = \frac{\mathbb{A}^2(\omega)}{\mathbb{A}^2(\omega) + \mathbb{B}^2(\omega)} g(\omega, r), \tag{A1a}$$

where

$$\left| \frac{\mathbb{A}(\omega_0)}{\dot{\mathbb{B}}(\omega_0)} \right| \leq 1 \qquad \text{and} \qquad \dot{\mathbb{B}} \equiv \frac{\mathrm{d}}{\mathrm{d}\omega} \mathbb{B}, \tag{A1b}$$

has a local maximum in the far-field, $r \gg 1$, at $\omega = \omega_0$, and $\mathbb{B}(\omega_0) = 0$, then $I(\omega, r)$ has a near-field maximum that is shifted with respect to the far-field maximum by

$$\Delta\omega(r) \approx \frac{1}{2} \frac{\dot{g}(\omega_0, r)}{g(\omega_0, r)} \left(\frac{\mathbb{A}(\omega_0)}{\dot{\mathbb{B}}(\omega_0)} \right)^2. \tag{A2}$$

To derive Eq. (A2), we first expand $I(\omega, r)$ in Taylor series around ω_0, i.e.,

$$I(\Delta\omega, r) \approx I(\omega_0, r) + \dot{I}(\omega_0, r)\Delta\omega + \frac{1}{2}\ddot{I}(\omega_0, r)\Delta\omega^2, \tag{A3}$$

and then maximize Eq. (A3) with respect to $\Delta\omega$ to obtain

$$\Delta\omega(r) = -\frac{\dot{I}(\omega_0, r)}{\ddot{I}(\omega_0, r)}. \tag{A4}$$

Through a straightforward but tedious exercise in differentiation, we also have

$$\dot{I}(\omega_0, r) = \dot{g}(\omega_0, r) \tag{A5a}$$

and

$$\ddot{I}(\omega_0, r) = \ddot{g}(\omega_0, r) - 2g(\omega_0, r) \left(\frac{\dot{\mathbb{B}}(\omega_0)}{\mathbb{A}(\omega_0)} \right)^2. \tag{A5b}$$

Substituting Eq. (A5) into Eq. (A4) and expanding the result in a formal power series in the small parameter $\mathbb{A}(\omega_0)/\dot{\mathbb{B}}(\omega_0)$ yields Eq. (A2). Note that to obtain Eq. (A2) we retained only the first term in the power series.

Funding. Ministerio de Ciencia e Innovación (MICINN) (FIS2013-45854-P); U.S. Army Research Laboratory (ARL) (W911NF-12-2-0019); United States Army International Technology Center Atlantic (USAITC-A) (W911NF-13-1-0245).

REFERENCES

1. J. A. Schuller, E. S. Barnard, W. Cai, Y. C. Jun, J. S. White, and M. L. Brongersma, "Plasmonics for extreme light concentration and manipulation," Nat. Mater. **9**, 193–204 (2010).
2. N. G. Khlebtsov and L. A. Dykman, "Optical properties and biomedical applications of plasmonic nanoparticles," J. Quant. Spectrosc. Radiat. Transfer **111**, 1–35 (2010).
3. S. Schlücker, "Surface-enhanced Raman spectroscopy: concepts and chemical applications," Angew. Chem. Int. Ed. **53**, 4756–4795 (2014).
4. A. N. Grigorenko, N. W. Roberts, M. R. Dickinson, and Y. Zhang, "Nanometric optical tweezers based on nanostructured substrates," Nat. Photonics **2**, 365–370 (2008).
5. J. Chen, P. Albella, Z. Pirzadeh, P. Alonso-González, F. Huth, S. Bonetti, V. Bonanni, J. Åkerman, J. Nogués, P. Vavassori, A. Dmitriev, J. Aizpurua, and R. Hillenbrand, "Plasmonic nickel nanoantennas," Small **7**, 2341–2347 (2011).
6. M. A. Kats, N. Yu, P. Genevet, Z. Gaburro, and F. Capasso, "Effect of radiation damping on the spectral response of plasmonic components," Opt. Express **19**, 21748–21753 (2011).
7. J. Zuloaga and P. Nordlander, "On the energy shift between near-field and far-field peak intensities in localized plasmon systems," Nano Lett. **11**, 1280–1283 (2011).
8. P. Alonso-González, P. Albella, F. Neubrech, C. Huck, J. Chen, F. Golmar, F. Casanova, L. E. Hueso, A. Pucci, J. Aizpurua, and R. Hillenbrand, "Experimental verification of the spectral shift between near- and far-field peak intensities of plasmonic infrared nanoantennas," Phys. Rev. Lett. **110**, 203902 (2013).
9. F. Moreno, P. Albella, and M. Nieto-Vesperinas, "Analysis of the spectral behavior of localized plasmon resonances in the near- and far-field regimes," Langmuir **29**, 6715–6721 (2013).
10. C. Menzel, E. Hebestreit, S. Mühlig, C. Rockstuhl, S. Burger, F. Lederer, and T. Pertsch, "The spectral shift between near- and far-field resonances of optical nano-antennas," Opt. Express **22**, 9971–9982 (2014).
11. A. J. Yuffa, P. A. Martin, and J. A. Scales, "Scattering from a large cylinder with an eccentrically embedded core: An orders-of-scattering approximation," J. Quant. Spectrosc. Radiat. Transfer **133**, 520–525 (2014).
12. A. B. Evlyukhin, C. Reinhardt, and B. N. Chichkov, "Multipole light scattering by nonspherical nanoparticles in the discrete dipole approximation," Phys. Rev. B **84**, 235429 (2011).
13. A. B. Evlyukhin, S. M. Novikov, U. Zywietz, R. L. Eriksen, C. Reinhardt, S. I. Bozhevolnyi, and B. N. Chichkov, "Demonstration of magnetic dipole resonances of dielectric nanospheres in the visible region," Nano Lett. **12**, 3749–3755 (2012).
14. Á. I. Barreda, J. M. Sanz, R. Alcaraz de la Osa, J. M. Saiz, F. Moreno, F. González, and G. Videen, "Using linear polarization to monitor nanoparticle purity," J. Quant. Spectrosc. Radiat. Transfer **162**, 190–196 (2015).
15. F. W. J. Olver, D. W. Lozier, R. F. Boisvert, and C. W. Clark, eds., *NIST Handbook of Mathematical Functions* (Cambridge University, 2010).
16. J. M. Sanz, R. Alcaraz de la Osa, Á. I. Barreda, J. M. Saiz, F. González, and F. Moreno, "Influence of pollutants in the magneto-dielectric response of silicon nanoparticles," Opt. Lett. **39**, 3142–3144 (2014).
17. G. Videen, J. Li, and P. Chýlek, "Resonances and poles of weakly absorbing spheres," J. Opt. Soc. Am. A **12**, 916–921 (1995).